



HAL
open science

Well injectivity during CO₂ storage operations in deep saline aquifers - Part 2: Numerical simulations of drying, salt deposit mechanisms and role of capillary forces

Laurent André, Yannick Peysson, Mohamed Azaroual

► To cite this version:

Laurent André, Yannick Peysson, Mohamed Azaroual. Well injectivity during CO₂ storage operations in deep saline aquifers - Part 2: Numerical simulations of drying, salt deposit mechanisms and role of capillary forces. *International Journal of Greenhouse Gas Control*, 2014, 22, pp.301-312. 10.1016/j.ijggc.2013.10.030 . hal-00932777

HAL Id: hal-00932777

<https://brgm.hal.science/hal-00932777>

Submitted on 17 Jan 2014

HAL is a multi-disciplinary open access archive for the deposit and dissemination of scientific research documents, whether they are published or not. The documents may come from teaching and research institutions in France or abroad, or from public or private research centers.

L'archive ouverte pluridisciplinaire **HAL**, est destinée au dépôt et à la diffusion de documents scientifiques de niveau recherche, publiés ou non, émanant des établissements d'enseignement et de recherche français ou étrangers, des laboratoires publics ou privés.

1
2
3
4
5
6
7
8
9
10
11
12
13
14
15
16
17
18
19
20
21
22
23
24
25

**Well injectivity during CO₂ storage operations in deep saline aquifers –
Part 2: Numerical simulations of drying, salt deposit mechanisms and role of
capillary forces**

Laurent André^a, Yannick Peysson^b, Mohamed Azaroual^a

^a*BRGM, Water Environment and Ecotechnologies Division, 3 Avenue Claude Guillemin,
BP 36009, F-45 060 Orléans Cedex 2 – France*

^b*IFPEN, 1-4 Avenue de Bois Préau, 92852 Rueil-Malmaison Cedex - France*

Submitted to

International Journal of Greenhouse Gas Control

26
27
28
29
30
31
32
33
34
35
36
37
38
39
40
41
42
43
44
45
46
47

Abstract

The injection of CO₂ into geological reservoirs or deep saline aquifers is being studied to control global warming by limiting greenhouse gas emissions. CO₂ is captured from exhaust gases in power plants or industrial units and stored in underground geological reservoirs. Return on experience with CO₂ injection in the oil industry clearly shows that injectivity problems can be encountered due to several mechanisms including mineral dissolution/precipitation and physical alteration due to the complete desaturation of the near-wellbore zone. This study describes numerical modelling that is able to reproduce the experimental results of drying of brine-saturated sandstone cores by gas injection in the laboratory. The evolution of water and gas saturation profiles and the precipitation of salt inside the samples are followed with injection time. Numerical results agree well with experimental observations highlighting the key role played by capillary forces during the desiccation process (see the companion paper; Peysson et al., 2013). A tentative extrapolation of experimental results from laboratory scale to the near-well field scale is proposed. This approach is of major importance because it makes it possible to determine the optimal CO₂ injection flow rate according to both the intrinsic petrophysical properties of the porous medium and initial brine salinities.

Keywords: supercritical CO₂, drying-out effects, coupled modelling, relative permeability.

48 **1. Introduction**

49 Geological sequestration of CO₂ in deep saline aquifers offers a promising solution for
50 reducing net emissions of greenhouse gases into the atmosphere. Nevertheless, this
51 emerging technology based on massive CO₂ injection in saline reservoirs can cause a major
52 disequilibrium of the physical and geochemical characteristics of the host reservoir. Recent
53 numerical simulations indicate that the near-well zone is the area most sensitive to and
54 impacted by the injection of supercritical CO₂. Geochemical reactions (e.g., CO₂ dissolution,
55 pH variation of original brine, mineral dissolution/precipitation) are expected to occur mainly in
56 this zone (Ennis-King and Paterson, 2007; Audigane et al., 2007; André et al., 2007, 2010;
57 Huq et al., 2012). Moreover, physical phenomena (e.g., variations in temperature, pressure,
58 gas saturation) will also generate major perturbations of the equilibrium of the host reservoir
59 (Bielinski et al., 2008; Kopp et al., 2009; Okwen et al., 2011, Menhert and Okwen, 2012;
60 Vilarrasa, 2012). Consequently, all of these processes might combine to enhance or alter its
61 initial porosity and permeability and long-term well injectivity. Detailed studies need therefore
62 to be carried out before effective gas injection in order to predict the sustainability of the
63 system and optimize the injection phase.

64 Among these perturbations, the desiccation of the porous medium appears to be a major
65 phenomenon with various positive or negative implications such as salt precipitation
66 (Peysson et al., 2010, Ott et al., 2010a, b), modifications of the local geomechanical
67 constraints and internal forces (Peter-Borie et al., 2011), and impacts of injected fluids on the
68 interfacial tensions including capillary/osmotic phenomena (Leroy et al., 2010). Desiccation
69 of porous media subjected to gas injection has been investigated at the laboratory scale on
70 cores (Mahadevan, 2005; Mahadevan et al., 2007; Peysson, 2012) and on a chip (Kim et al.,
71 2013). This process has also been observed at the field scale during the injection of dry gas
72 into oil and gas reservoirs (Kleinitz and Tölcke, 1982; Kleinitz et al., 2001, 2003; Vandeweyer
73 et al., 2011). Salt deposits cause a pressure draw-down in injection wells or decrease
74 productivity in production wells. The modelling of CO₂ storage in deep saline aquifers has

75 emphasized the importance of drying mechanisms on injectivity (Pruess and Muller, 2009;
76 Giorgis et al., 2007; Hurter et al., 2007; André et al., 2007; Zeidouni et al., 2009; Alkan et al.,
77 2010) and has led to new research efforts on that topic.

78 Mechanistically, the massive and continuous injection of CO₂ in an initially saturated porous
79 medium causes water displacement and evaporation. First, mobile water is pushed out by
80 the injected supercritical CO₂ according to two-phase displacement (brine - CO₂). At the end
81 of this phase, immobile residual water trapped in pores or distributed on grain surface as thin
82 films comes in contact with the flowing dry CO₂. Consequently, a continuous and extensive
83 evaporation process leads both to the formation of a reactive drying front moving into the
84 medium, and the precipitation of salts and possibly secondary minerals in residual brines
85 (Mahadevan et al., 2007). This desiccation and the following salt precipitation are also highly
86 influenced by capillary forces, which draw the brine towards the injection points (Giorgis et
87 al., 2007).

88 This study investigated the consequences of near-wellbore drying-out on well injectivity
89 through the evolution of the petrophysical properties of the porous medium. The objective
90 was to determine the key processes controlling the drying of the porous media during the
91 injection of dry gas, and identify the parameters needed to predict the behaviour of the salt
92 (dissolved and solid) inside the core. Our understanding of these processes is essential for
93 the long-term management of the evolution of gas injection into the reservoir.

94 The work involved both laboratory experiments and numerical modelling. The drying potential
95 of a gas phase was studied in the laboratory on sandstone plugs (6 cm in length and 4.9 cm in
96 diameter) (Peysson et al., 2013). These experiments were then interpreted using a numerical
97 modelling approach coupling hydraulic, thermal and thermodynamic processes able to
98 simulate the evolution of liquid and gas saturation in time and space. A very fine
99 discretization of the plugs enabled us to capture the continuous evolution of water, gas and
100 salt profiles in the porous medium and estimate the porosity and permeability variations
101 during the drying process.

102 The parameters established at the centimetre scale were then used without modification in
 103 order to extrapolate the results at the near-wellbore scale and predict the impact of
 104 CO₂ injection on the petrophysical properties of the host rock. A precise description of fluid
 105 (gas and water) flows inside the reservoir enabled us to identify the key processes, and, for
 106 given rock properties, the clogging risks due to salt precipitation related to the CO₂ injection
 107 flow rate.

108 2. EXPERIMENTAL APPROACH AT THE LABORATORY SCALE

109 2.1 Rock samples: characterization and hydraulic properties

110 Vosges sandstones were selected for this study because it is a rock-type representative of
 111 the Triassic formations from Eastern part of Paris Basin (France), which were identified as
 112 potential reservoirs for CO₂ storage (Sterpenich et al., 2006). Vosges sandstones, also well-
 113 known for their homogeneity, were sampled in a quarry. It is composed of quartz (70 - 80 %),
 114 microcline (10 -20 %) and about 10 % of a mixture of muscovite, albite, smectite, anorthite
 115 and hematite (Sterpenich et al., 2006). Cylindrical cores 6 cm in length and 2.5 cm in
 116 diameter are prepared from the sampled block.

117 The hydraulic properties of Vosges Sandstones were characterized: porosity (Φ) and
 118 permeability (K_0) were 21.8 % and 74 mD, respectively. A high pressure mercury injection
 119 was used to measure the pore throat distribution (Peysson, 2012). This injection also allowed
 120 determining the gas-water capillary pressure curve (Fig. 1).

121 For next numerical simulations, a standard Corey model (Corey, 1954) was used to
 122 represent relative permeability curves of both the liquid (k_{rl}) and gaseous (k_{rg}) phases, and a
 123 Van Genuchten model (Van Genuchten, 1980) was used to fit the experimental capillary
 124 pressure (P_{cap}) curve (Fig. 1):

$$125 \quad k_{rl} = \hat{S}^r \quad \text{and} \quad k_{rg} = (1 - \hat{S})^p \quad \text{with} \quad \hat{S} = \frac{S_l - S_{lr}}{1 - S_{lr} - S_{gr}} \quad (1)$$

126 where S_l , S_{lr} and S_{gr} are the liquid saturation, the irreducible liquid saturation and the
127 irreducible gas saturation, respectively. For the Vosges Sandstone sample, $r = 5.5$ and $p = 2$.
128 The irreducible water saturation (S_{lr}) was 0.19 and the irreducible gas saturation was nil.

129
$$P_{cap} = -P_0 \left([S^*]^{1/m} - 1 \right)^{1-m} \quad \text{with} \quad P_0 = 1.82 \cdot 10^4 \text{ Pa} \quad ; \quad m = 0.675 \quad ; \quad S^* = \frac{S_l - S_{lr}}{S_{ls} - S_{lr}} \quad (2)$$

130 All the parameters used in Eq. (1) and (2) were adjusted from different drainage capillary
131 curves recorded on Vosges Sandstone cores (results not shown here). Specific efforts were
132 made in particular to estimate P_0 , the entry pressure, because it is a key parameter in the
133 prediction of the gas breakthrough. The selected value of 182 mbar was in agreement with
134 values proposed by Peysson (2012).

135 *2.2 Brine and non-wetting fluid*

136 Before experiment, Vosges sandstone cores were fully saturated with brine composed of 55
137 % KCl and 45 % KI, the latter intensifying the density contrast for X-ray measurements.
138 According to experiments, water salinity was 35 and 150 g/L.

139 The first objective of this work was to determine the drying potential of the gas phase on
140 sandstone plugs. The best solution was to use CO_2 in a supercritical state (i.e. at pressures
141 greater than 7.4 MPa and temperatures higher than 31.1 °C). But, because of experimental
142 constraints (stability of large volumes of $\text{CO}_{2,sc}$, maintenance of the devices, problems of
143 injection...), nitrogen replaced $\text{CO}_{2,sc}$ as the non-wetting fluid and temperature and pressure
144 were set to 80°C and 50 bars, respectively. In these conditions nitrogen is a gas with drying
145 properties close to those of CO_2 (as explained in paragraph 3.1). The experimental results
146 with N_2 on core drying were thus comparable with those obtained on experiments performed
147 with CO_2 .

148

149

2.3 Experimental setup

In the laboratory, nitrogen was injected into Vosges sandstone cores encapsulated in X-ray transparent cells and placed in an oven under controlled temperature (80 °C) (Fig. 2). The cell is composed of a membrane in order to confine the core at a pressure of 50 bar. Experiments are performed by applying, between the inlet and the outlet of the column, increasing pressure plateaus in one case, and a constant pressure difference in other. The local water saturation in the sample was measured during the injection of dry gas (nitrogen) with X-ray attenuation techniques. The experiments continued until the cores were completely dry. The volume of water expelled was measured in a burette at the column outlet, and a gas flow meter recorded the outlet gas flow rate (Peysson et al., 2010, 2013; Peysson, 2012). Gas permeability and porosity profile of cores were measured at the beginning and at the end of the experiment to evaluate the role of the drying.

2.4 Experimental results

For the first experiment, three pressure plateaus (120 mbar, 800 mbar and 1500 mbar) were imposed to the core initially saturated with a 35 g/L of brine (Peysson et al., 2013). During the first one, a two-phase flow displacement occurred with a rapid gas breakthrough (at $t = 5$ hours) and a low gas flow rate (Fig. 4). The saturation profile in the core showed a typical capillary fringe close to the outlet of the sample. During the second plateau, core continued to desaturate, with a significant contribution of drying. The saturation profiles are flatter because of capillary back flows. For the highest pressure, drying is very rapid, lasting only a few hours. During this phase, a drying front moved from the inlet to the outlet of the core. The dissolved salt, initially present in the brine and transported in the capillary flows, accumulated as precipitate near the injection surface, involving a decrease of about 70 % of the initial permeability.

For the second experiment, a constant difference pressure (300 mbar) was imposed to the core initially saturated with a 150 g/L of brine. A rapid gas breakthrough was observed (less

176 than 2 hours) with an increase of the gas flow rate up to 26 hours. Then a plugging of the
177 core occurred with no gas flow after 46 hours. The salt accumulation near the injection
178 surface generated by capillary back flows was sufficient to block the gas flow.

179 **3. MODELLING TOOLS AND NUMERICAL PARAMETERS**

180 TOUGH2 (Pruess et al., 1999) was used for all of the numerical simulations done in this
181 study (core experiments and field scale). This code couples thermal and hydraulic processes
182 and is applicable to one-, two-, or three-dimensional, physically heterogeneous geologic
183 systems. It is a modular code that can be adapted to a broad range of applications by simply
184 using interchangeable calculation modules. Two modules were used for this study:

185 - The EOS7C module (Oldenburg et al., 2004) is a fluid property module developed
186 specifically to deal with mixtures of non-condensable gases (like CO₂ or N₂) and methane. It
187 can be used to model isothermal or non-isothermal multiphase flow in water/CH₄/(CO₂ or N₂)
188 systems. This module uses a cubic equation of state and an accurate solubility formulation
189 along with a multiphase Darcy's Law to model flow and transport of gas and aqueous phase
190 mixtures over a wide range of temperatures and pressures (See Appendix A).

191 - The ECO2n module (Pruess, 2005) is specifically developed to model isothermal or non-
192 isothermal multiphase flow in water/brine/CO₂ systems in deep geological reservoirs
193 (aquifers or depleted gas fields). It is based on the equilibrium between the supercritical
194 phase and the aqueous phase assumed for CO₂ dissolution. Hence,



196 where(sc) and (aq) denote supercritical and aqueous carbon dioxide, respectively. An
197 extension of Henry's Law is used to estimate the dissolution of CO₂:

$$198 \quad K_{FP} = \gamma C \quad (4)$$

199 where K is the equilibrium constant depending on the temperature T , P is the partial pressure
200 of CO_2 , γ is the aqueous CO_2 activity coefficient, C is the aqueous concentration (mol/kg
201 H_2O), and Γ is the fugacity coefficient depending on pressure and temperature.

202 3.1 Thermodynamic properties of non-wetting fluids (CO_2 and N_2)

203 Although our objective is to predict the behaviour of carbon dioxide, laboratory experiments
204 were done with nitrogen in order to avoid ancillary geochemistry mechanisms and focus on
205 the physical effects of drying. Calculations were therefore done to estimate the
206 thermodynamic behaviour of CO_2 and N_2 and determine how the nature of the fluid might
207 impact the desaturation process. Simulis© Thermodynamics, a code developed by PROSIM
208 S.A. (<http://www.prosim.net>), was used to define the fraction of water in the two phases (CO_2
209 and N_2) according to temperature at 80 °C (Fig. 3). The code integrates various equations of
210 state such as the Peng-Robinson (PR) equation used here for CO_2 and N_2 . The coefficients
211 $K_{i,j}$ used for calculations are those of Soreide and Whitson (1992). The curves obtained with
212 the PR equation were compared to the curve obtained with the Raoult Law (assimilation of
213 N_2 and CO_2 to perfect gases):

$$214 \quad y_{\text{H}_2\text{O},\text{gas}} = \frac{P_{\text{water},\text{sat}}}{P} \quad (5)$$

215 where P and $P_{\text{water},\text{sat}}$ are the total pressure and the saturated vapour pressure of water,
216 respectively, calculated with the IAPWS95 equation of state (Wagner and Pruss, 2002). The
217 fraction of water in the supercritical CO_2 phase is higher than in the N_2 phase (about 30 % at
218 50 bar and 80 °C), whereas the N_2 curve is close to the Raoult curve, indicating that N_2 can
219 be assimilated to a perfect gas in this range of temperature and pressure (Fig.3). In a first
220 approximation, the substitution of N_2 by CO_2 in the modelling phase has a limited impact on
221 the results since the evaporation potentials of the two fluids are similar in these pressure and
222 temperature ranges. Only a shorter desaturation time is expected using CO_2 . Moreover, the
223 type of gas in the model can be changed by calculating the proper thermodynamic
224 coefficients.

3.2 Modelling core experiments

Two sets of calculations were done to study the experimental results. The first set consisted in using the EOS7C module of the TOUGH2 code to simulate the injection of nitrogen with increasing pressure-steps into a brine-saturated sandstone plug (Fig. 2 and Peysson et al., 2013) in order to determine the time required to desiccate the porous medium and estimate the gas flow rates at the outlet of the core as a function of pressure and temperature (see paragraph 2). A two-phase Darcy's flow equation was solved using relative permeability and capillary pressure curves. Thermodynamic equilibrium between concomitant phases (water- N_2), similar to the Eq. (3) defined for CO_2 , assumes that phase exchanges are responsible for the core drying. This thermodynamic equilibrium is calculated at each time step to determine the water vapour fraction in the gas phase and the fraction of dissolved gas in the brine.

The EOS7C module (version 1.0) does not take into account the salinity of the brine, i.e., it cannot determine either the solubility of the gas in the brine according to its salinity or the amount of salt precipitated inside the core (Oldenburg et al., 2004). Consequently, an additional set of calculations were done with the ECO2n module in order to determine the quantity and location of the salt deposited in the core. In this simulation, CO_2 was injected instead of N_2 . This simulation was also used to fit the most influential parameters, such as the relationship between porosity and permeability.

In a second set of calculations, the same procedure was used to study the impact of a constant gas injection flow rate and determine the influence of the desaturation path on the deposit locations inside the core.

A 1D-column model 60mm long was used as a conceptual framework for determining the evolution of the water content induced by the injection of N_2 and CO_2 in both time and space. The column was represented by 60 grid blocks making up the mesh. Each grid cell was 1.0 mm thick. In the lab experiments, the core was cylindrical, whereas in the model, the core is a parallelepiped. The section of the parallelepiped is therefore recalculated to obtain the same

252 pore volume as the original cylindrical sample. The porous medium (rock matrix) is assumed
253 to be inert with respect to N_2 and CO_2 , i.e. no chemical reactivity. In the next simulations of
254 lab experiments, the initial brine saturating cores only contains sodium chloride.

255 *3.3 Modelling field applications*

256 Two sets of calculation were done to study the field scale. In the first set, a 1D-radial model
257 was used as a conceptual framework for determining the transient evolution of the water
258 content induced by the injection of supercritical CO_2 (considered to be a non-wetting fluid).
259 The generic 1 m-thick reservoir was centred around a vertical injection well. The maximum
260 explored radial distance was 100 km. Along the radius axis, the discretization was very fine
261 close to the well (5 1-mm grid cells, then 5 2-mm grid cells, 77 5-mm grid cells, and 960 10-
262 mm grid cells up to 10 m from the injection well). There were 100 grid cells between 10 and
263 100 m, 100 grid cells between 100 m and 10 km, and 20 grid cells thereafter, up to 100 km.
264 In each interval (between 10 m and 100 km), the width of radial elements followed a
265 logarithmic scale. The objective of such refinement near the injection well was to capture
266 more precisely both the details and the migration of the desiccation front in the near-well
267 region.

268 In the second set of calculations, a 2D-radial model was used to complement the 1D-radial
269 studies and to include gravity effects. The reservoir was 20 m thick and had a homogeneous
270 structure. The discretization along the radius axis was the same as the one used for the 1D-
271 radial model.

272 For both calculations, porosity was 21.8 %, $K_h = 74$ mD and $K_v = 7.4$ mD ($K_v / K_h = 0.1$). The
273 reservoir was initially fully saturated with sodium chloride brine. Capillary and relative
274 permeability curves are given in figure 1. The initial temperature and pressure of the targeted
275 reservoir were 80 °C and 180 bar, respectively. No regional flow was considered and a
276 hydrostatic status was initially assumed for the pressure in the reservoir and maintained
277 constant at the lateral boundary.

278 For the 1D-radial model, different injection flow rates were used and their impact on the near
279 wellbore integrity was estimated according to the intrinsic rock properties. This was done to
280 estimate the mechanisms able to influence well injectivity. For the 2D-radial model, the
281 injection lasted 10 years with an injection flow rate of 1 kg/s, distributed on the entire
282 thickness of the reservoir. This is the equivalent of a specific flow rate of 0.050 kg/s/m (total
283 amount of injected CO₂ = 315.36 kt).

284 **4. Results and Discussions**

285 *4.1 Modelling core experiments*

286 ***Core drying and salt precipitation for desaturation with pressure-steps***

287 Simulations with TOUGH2's EOS7C module involved modeling the N₂ injection in brine-
288 saturated sandstone cores. The salinity of sodium chloride brine was 35 g/L. Three pressure
289 plateaus ($\Delta P = 0.12, 0.80$ and 1.50 bars) were applied between the inlet and the outlet of the
290 column to progressively dry the core. The mean water saturation (calculated from the water
291 saturation in each 1-mm core slice) and the outlet gas flow rates were calculated throughout
292 the injection period, for each pressure step. Results obtained with numerical simulations
293 agree well with experimental data (Fig. 4). During each pressure step, the mean water
294 saturation was well predicted and the value obtained at the end of the second step (for $t = 40$
295 hours) was coherent with the irreducible water saturation ($S_{ir} = 0.19$). This means that all the
296 mobile water was removed from the core, leaving only the residual water inside the medium.

297 Despite the application of a low pressure difference, the approaches used were sensitive
298 enough to reproduce the overall evolution of the system, even the outlet gas flow rate. The
299 model was able to accurately determine not only the gas breakthrough time at the end of step
300 1, but also the gas flow rate, regardless of the water saturation inside the column (even when
301 the column is dry).

302 At the end of the nitrogen percolation experiment, X-ray measurements revealed the
 303 precipitation of salt (halite) inside the porous medium. The new estimated permeability was
 304 about 22 mD compared to the initial permeability of 74 mD, i.e. a reduction of about 70% due
 305 to salt precipitation. Salt precipitation appears to be heterogeneous inside the core, with salt
 306 accumulating near the injection surface (Peysson, 2012; Peysson et al., 2013).

307 This precipitation process was modeled with TOUGH2's ECO2n module (see Appendix B).
 308 However, to understand the evolution of the permeability inside the core, a relationship
 309 between porosity and permeability needs to be selected. Verma and Pruess's "tube-in-
 310 series" model (1988) was used because it allows us to reach zero permeability even if
 311 porosity is not nil, as experimentally observed. It uses the fraction of pore space occupied by
 312 precipitated salt and two other parameters: Π , the fractional length of pore bodies and ϕ_r , the
 313 fraction of initial porosity for which permeability is reduced to zero. The evolution of
 314 permeability K , according to the initial permeability K_0 is given by:

$$k_{red} = \frac{K}{K_0} = \theta^2 \cdot \frac{1 - \Pi + \Pi / \omega^2}{1 - \Pi + \Pi [\theta / (\theta + \omega - 1)]^2}$$

315 where (6)

$$\theta = \frac{1 - S_s - \phi_r}{1 - \phi_r} \quad \text{and} \quad \omega = 1 + \frac{1 / \Pi}{1 / \phi_r - 1}$$

316 where S_s is the solid saturation, i.e. the pore space volume occupied by precipitated salt.
 317 Usually, $\Pi = \phi_r = 0.80$ as given in Pruess et al. (1999) and by various other authors (Alkan et
 318 al., 2010).

319 Calculations done with these Π and ϕ_r values underestimated the decrease in permeability. The
 320 values were therefore modified and optimized in order to fit a decrease in permeability
 321 coherent with experimental data. This was achieved with $\Pi = 0.80$ and $\phi_r = 0.91$, i.e. a drastic
 322 decrease in permeability for a low decrease in porosity (Fig. 5). These values are not out of
 323 range since they have already been used in a geothermal field in the Philippines where silica
 324 scaling causes high permeability decreases (Xu et al., 2004). These results are also in
 325 agreement with the values obtained by Peysson (2012).

326 Calculations done with these new parameter values gave a decrease in permeability of
327 around 55-60 % of the initial permeability, which is not too far from the 70% determined in the
328 experiment. The mean permeability was about 31 mD (compared to an initial 74 mD), with
329 some variations around this value probably due to the boundary conditions chosen for these
330 simulations (Fig. 6). The total amount of precipitated salt was about 1.73 g (compared to the
331 3.73 g of salt initially dissolved in the original pore water). Figure 6 also shows a large
332 decrease in permeability in the first millimetre, as observed in the experiments. This is due to
333 the accumulation of salt close to the injection zone in agreement with X-ray adsorbance
334 measurements (Fig. 7) (Peysson et al., 2013).

335 The interpretation of these results enabled us to determine the k/Φ relationship. The
336 objective was then to apply this approach to another kind of simulation and to determine
337 whether the results of numerical simulations were in agreement with experimental
338 observations.

339 ***Salt precipitation for desaturation with a constant pressure difference***

340 A sandstone core saturated with brine enriched in KCl (150 g/L) was dried in the laboratory
341 with a constant pressure difference. The nitrogen flow rate at the outlet of the core decreased
342 to zero during the experiment, which shows that clogging occurred inside the core (Peysson,
343 2012; Peysson et al., 2013). This experiment was modeled with the ECO2n module, by
344 injecting CO₂ with a constant pressure difference of 0.3 bar. The previously determined k/Φ
345 relationship was used to simulate the loss of permeability generated by the deposition of salt
346 inside the core. In the simulation, because of sodium chloride brine, the precipitation of halite
347 is examined.

348 The precipitation profile obtained numerically shows zero permeability close to the injection
349 point and relatively high values close to the column outlet (Fig. 6). About 1.81 g of salt
350 precipitated – 1.11 g in the first half of the column and 0.70 g in the second half, indicating a
351 massive precipitation close to the column inlet.

352 Figure 7 shows that salt accumulated in the first millimeters of the core, close to the injection
353 zone. This explains the clogging observed in our experiments (permeability reduced to
354 zero). The results were compared to those obtained in the previous experiment, i.e. the drying
355 according to pressure steps. The shapes of the curves are the same, with a homogeneous
356 deposition of salt throughout the columns, except in the first millimeters where there is
357 clogging. This can be explained by fluid (non-wetting and water) displacement inside the
358 core. Numerical calculations showed that:

- 359 - Before the gas reaches the column outlet, both fluids (water and non-wetting) move
360 from the inlet to the outlet of the core. Gas is injected in the column and pushes “free”
361 water out of the core.
- 362 - When the gas flow rate is measured at the outlet of the core (i.e. when the column is
363 partially desaturated), the gas continues to move from the inlet to the outlet of the
364 column, whereas water moves in the other direction.

365 Gas injection results in water back-flow inside the desaturated core due to capillary forces.
366 This transports dissolved salt towards the injection point where evaporation is a predominant
367 mechanism. Consequently, a large amount of salt precipitates, accumulates and has an
368 impact on porosity and then on permeability.

369 The influence of the injection flow rate on the amount of salt deposited in the core cannot be
370 assessed with these two experiments because the brines used did not have the same initial
371 salinity. This is, however, discussed below.

372 *4.2 Modelling at field scale (1D-radial approach)*

373 In order to understand multiphase flow during CO₂ injection in saline aquifers, we
374 extrapolated to field scale, first with a 1D and then with a 2D radial model (see paragraph
375 3.3). For these simulations, we considered that the set of k_r - P_c parameters used for predictive
376 simulation at the core scale would enable modeling of CO₂ injection at the reservoir scale.
377 Bennion and Bachu (2005) advised that relative permeability characteristics have to be

378 determined under reservoir conditions to accurately parameterize reservoir models.
379 However, Egermann et al. (2006) demonstrated that both experiments and large scale
380 applications can be simulated using a single set of parameters. The predictive model for CO₂
381 injection at the reservoir scale is sufficiently accurate if gas-water relative permeability curves
382 and thermodynamic data (solubility of CO₂ in the liquid water phase and water vapour
383 pressure in the CO₂ gas phase) are taken into account in the model. Since TOUGH2 code
384 uses the thermodynamic and thermophysical properties (density, viscosity and enthalpy) of
385 the non-wetting CO₂ phase and the k_r - P_c curves for simulations, we used, as an
386 approximation, a single set of parameters to extrapolate to the reservoir scale.

387 Numerical simulations were then done at 180 bar and 80 °C, although the P_c curve was
388 drawn for 50 bars and 80 °C. The P_c curve could have been modified using the Leverett
389 function to take into account this difference in pressure. However, since the gas-brine
390 interfacial tension (IFT) between 50 and 180 bars does not change considerably (Chiquet et
391 al., 2007; Chalbaud et al., 2009), the P_c curve shown in figure 1 was used in a first
392 approximation.

393 The 1D numerical simulations were done to study the possible correlation between brine
394 salinity (sodium chloride content), CO₂ injection flow rate and the spatial distribution of salt
395 (halite) precipitation. Sensitivity calculations are done to test the behavior of the system with
396 respect to these parameters. First, CO₂ was injected into a reservoir containing brine. Two
397 salinities were tested, 10 and 100 g/L, while the same over pressure was applied between
398 the well and the reservoir ($\Delta P = 2$ bars, equivalent to a mean injection flow rate of about
399 0.015 kg/s/m).

400 As expected, based on the core scale experiments, supercritical CO₂ injection caused the
401 drying of the porous medium around the well, but results differed depending on brine salinity.
402 The impact on permeability was much greater for the more concentrated brine, with probable
403 clogging near the injection point (Fig. 8). The impact on permeability was not limited to the
404 near-well zone but extended inside the reservoir formation. These calculations show that the

405 amount of precipitated salt is directly related to the salinity of the brine initially present in the
406 porous medium.

407 Simulations were also done to determine whether clogging might be prevented with a
408 different injection flow rate. The same simulation as above was done with three different
409 pressure differences between the well and the reservoir. For low salinities (10 g/L) and $\Delta P >$
410 5 bars (for a mean injection flow rate > 0.045 kg/s/m), salt precipitation affected the
411 permeability of the porous medium only slightly (about 5 % decrease in permeability) (Fig.
412 9a). When the injection pressure decreased (low ΔP and low injection flow rates of around
413 0.010 to 0.015 kg/s/m), the quantities of precipitated salts increased and the near wellbore
414 porous medium became clogged when the injection flow rate was lower than 0.010 kg/s/m.

415 For higher brine salinities (100 and 160 g/L), the application of strong over pressure ($\Delta P = 15$
416 to 40 bars, equivalent to mean injection flow rates of about 0.120 to 0.500 kg/s/m) caused
417 the precipitation of salts around the injector well, decreasing the permeability by about 40
418 and 60 % for brine salinities of 100 and 160 g/L, respectively (Fig. 9a). When the over
419 pressure decreased (injection flow rates lower than 0.030 to 0.050 kg/s/m depending on
420 brine salinity), salt precipitation increased up to the clogging of the near wellbore domain.

421 The over pressure used to inject CO_2 needs, therefore, to be adapted to the salinity of the
422 native aqueous solution and the petrophysical properties (K , k_r , P_c and ϕ) of the host
423 reservoir. This sensitivity study showed that when the CO_2 injection flow rate is too low, a
424 porous medium could become clogged near the injection well even in the presence of a low
425 salinity-brine. An analogy can be made between the gas flow rate and the Péclet number (Pe)
426 reported by Peysson (2012) and Peysson et al. (2013). For each salinity/injection flow rate
427 couple, there is a threshold gas flow rate (Q_i) and a limit Péclet number (Fig. 9b). For the
428 Vosges sandstone, a brine salinity of 10 g/L entails a threshold gas flow rate of about 0.010
429 kg/s/m (equivalent to a Péclet number of 430), whereas for higher brine salinity, Q_i increases
430 up to 0.030 kg/s/m ($Pe = 1200$) and 0.050 kg/s/m ($Pe = 2000$) for salinities of 100 g/L and 160
431 g/L, respectively. Below these threshold values, the system clogs due to the capillary back

432 flow that moves brine (and dissolved salts) toward the injection point generating/stabilizing
433 an evaporation aureole accumulating salt deposits. The water is evaporated by the
434 continuous injection of gas, leaving solid salt behind reducing permeability to zero according
435 to the k/Φ relationship used for this sandstone. These numerical results are in agreement
436 with laboratory experiments done with this Vosges sandstone (Peysson et al., 2013). These
437 authors observed a clogging of the core with a brine salinity of 150 g/L and $Pe = 360$.
438 However, when the injection flow rate was higher than the threshold value, two-phase
439 displacement seems to be the main process – the water saturation close to the injection
440 surface was sufficiently low to decrease the capillary back flow and limit the back flow of
441 dissolved salts. Salt precipitation near the injection point was thus lowered and salts tended
442 to be deposited farther from the sensitive and strategic near-wellbore zone. Salt precipitated
443 more homogeneously throughout a large near-wellbore zone, decreasing the global
444 permeability of the medium but not clogging the core. In all of these calculations, salt
445 diffusion was disregarded. Indeed, given the high Péclet number values, this hypothesis is
446 valid.

447 *4.3 Modelling at field scale (2D-radial approach)*

448 A 2D-radial system was considered in order to develop an integrated approach able to
449 represent the coupling of different thermodynamic mechanisms (such as the evaporation of
450 brine and the equilibrium between gas and liquid phases) and physical processes (such as
451 the transport of a non-wetting supercritical fluid in a saline reservoir, gravity and capillary
452 forces, etc.). We simulated the uniform and continuous injection of CO_2 along the entire
453 thickness of the reservoir for 10 years. The reservoir was initially saturated with sodium
454 chloride (NaCl) brine with a salinity of 160 g/L. The specific injection flow rate used (0.050
455 kg/s/m) was voluntarily close to the Q_t value defined for the 1D-radial model. The objective
456 was to determine whether the clogging predicted by the 1D-radial model for this injection flow
457 rate and brine salinity also occurs on the 2D-radial model.

458 Because of gravity forces and the supercritical CO₂ density (lower than that of the brine), the
459 reservoir dries out faster at the top. Figure 10a clearly shows that the porous medium is dry
460 over about 12 m at the top of the reservoir, whereas only the first meter is dry at the bottom.
461 Inside the drying zone, solid salt (i.e., halite) precipitates. Although salt is present in all of
462 the desaturated zone, the spatial distribution of salt deposits varies according to the prevalent
463 transport forces (advection, diffusion, capillarity, evaporation, etc.) inside the reservoir: the
464 quantities are higher at the bottom of the reservoir and more limited at the top (Fig. 10b) for
465 simulation conditions and the specific characteristics of the reservoir. The pattern of solid
466 saturation (= solid volume/pore volume) indicates that 40 % of the porosity is filled with salt at
467 the bottom, whereas only 10 % is filled at the top. According to the k/Φ law established in
468 paragraph 4.1, the porosity and consequently the permeability are more impacted at the
469 bottom of the reservoir (Fig. 10c). The decrease in permeability is represented by the
470 empirical function k_{red} (= K/K_0). This function clearly shows that high permeability
471 reductions are expected near the well (skin effect in the cells adjacent to the well) and in the
472 lower part of the reservoir (in the first meter inside the reservoir).

473 To explain this distribution of salt inside the reservoir and the massive deposits at the bottom
474 of the aquifer, it is necessary to plot the fluid flows inside the reservoir. Figure 11 shows the
475 directions and trajectories of gas (a) and brine (b) flow inside the reservoir, which initially had
476 a homogeneous structure and petrophysical properties that facilitated fluid circulation
477 throughout the entire thickness (20 m). The lengths of the flow vectors drawn for each grid
478 cell are proportional to the intensity of the flow. The arrows show direction. The vectors are
479 centered on the grid cells.

480 CO₂ vectors are oriented from left (the well) to right, with some deviation towards the top of
481 the reservoir (Fig. 11a). The vertical permeability, ten times lower than the horizontal
482 permeability, limits upward flow, but this is clearly seen in this figure. This figure also shows
483 that gas fluxes are higher in the upper part of the reservoir (between $z = 10$ and 20 m), which
484 explains the shorter time required to desaturate this zone and its lateral extension.

485 Brine fluxes in the reservoir are more complex (Fig. 11b). Trends differ depending on the
486 location in the aquifer. Close to the well and within a radius of about 30 m, brine flows toward
487 the injector whereas the gas phase flows away from it. Far from the well, the water flows
488 from left to right and from up to down. Beyond 30 m, the gas phase displaces the water by a
489 piston effect from left to right and, because the gas phase is less dense, the brine is pushed
490 downwards, the size of the arrows indicating the intensity. Close to the well (0-30 m), brine
491 flows towards the injection well. Saline water flows towards the well due to capillary forces
492 that compete with the evaporation process. The length of the arrows shows that the highest
493 flows are at the bottom of the reservoir. In this reservoir zone, capillary forces are great
494 enough to move water in grid cells very close to the well. These flows move the water,
495 which is then evaporated by the continuous injection of desiccant fluid (CO_2), depositing
496 large quantities of salt in this region. At the top of the reservoir, the capillary brine back flows
497 are weaker and less salt is therefore deposited.

498 This simulation shows that a CO_2 injection specific flow rate of 0.050 kg/s/m causes the
499 clogging of the porous medium in the lower part of the reservoir where capillary brine flows
500 are higher (in agreement with 1D-radial model results). As expected from laboratory
501 experiments, the permeability is clogged by salt deposits because of the injection flow rate
502 which is below the Q_t value. These results were obtained for a homogeneous reservoir 20-m
503 thick (Figure 12). Although clogging occurs in the lower part of the reservoir, the well
504 injectivity is only moderately altered. However, reservoirs are usually highly heterogeneous
505 and very often made up of thick layers separated by less permeable layers that limit vertical
506 flow. Gas cannot move vertically. Consequently, each reservoir compartment can be
507 considered to be a 1D case with major horizontal gas flows and capillary effects in each sub-
508 domain. Clogging risks are increased in each compartment with a potentially strong impact
509 on well injectivity.

510 This study clearly shows that a specific integrated approach is necessary in order to take into
511 consideration both thermodynamic mechanisms and physical processes and adapt injection
512 conditions to reservoir properties.

513 **5. Conclusions**

514 Drying processes were studied with laboratory experiments and numerical simulations in
515 order to determine the dynamics of the decrease in water saturation in sandstone and the
516 consequences of induced salt depositions on rock permeability. Experiments at the
517 laboratory scale revealed the major role played by capillary forces and the salinity of the
518 initial brine on the changes in permeability. These experiments also highlighted the
519 relationship between salt deposits, gas injection flow rate and the capillary properties of the
520 porous medium subjected to non-wetting fluid injection, and demonstrated the need to use a
521 coupled and dynamic approach to fully represent the mechanisms involved.

522 The numerical code used in this study was able to accurately reproduce both the evolutions
523 of the water content in sandstone cores and the salt precipitation with a given brine salinity
524 and various CO₂ injection flow rates. The thermodynamic and physical processes were well
525 simulated at small scale on a homogeneous porous material.

526 Based on our experimental results (rocks characteristics) and several hypotheses (such as
527 the extension of k_r/P_c curves obtained at laboratory scale to a large scale, the homogeneity
528 of the reservoir), this study also investigated the behaviors of water, salt and a non-wetting
529 fluid at the reservoir scale, and more precisely in the near-well zone. This integrated
530 approach combining experimental and numerical simulations showed that the salt
531 precipitation process and the amount of salt deposited are related to various parameters
532 such as the salinity of the initial brine. The higher the brine concentration, the greater the salt
533 deposit. However, the location of the deposits inside the reservoir is strongly linked to the
534 supercritical non-wetting fluid injection flow rate and the capillary forces generating back-
535 flows. The numerical simulations showed that the capillary properties of the rock prevent a

536 sudden evaporation of the irreducible water by continuously feeding the injection zone with
537 “new” brine coming from reservoir zones far from the injection well. However, a sufficiently
538 high gas injection rate can overcome the capillary forces and limit the precipitation of salts
539 close to the injection well. Sensitivity analysis made it possible to determine a threshold gas
540 flow rate (Q_t) dependent on brine salinity. Below this threshold value, there is a high risk of
541 clogging, whereas higher values ($Q > Q_t$) can reduce the risk of clogging. However, if high
542 gas injection flow rates in high saline aquifers can prevent clogging, decreased permeability
543 is expected, even far from the injection well zone.

544 This study highlights that all these parameters (kr/P_c curves, brine salinity, pressure and CO_2
545 injection flow rates) must be known in order to improve the management of the industrial
546 injection of CO_2 in saline aquifers. The real structure of the reservoir as its heterogeneity (not
547 considered in this study) has also to be taken into account as a key parameter because it
548 could modify the capillary fluxes and thus, the localisation of the salt deposits.

549 **Acknowledgements**

550 This work was carried out within the framework of the “ProchePuits” project, co-funded by the
551 French National Agency for Research (ANR). The authors thank Marc Parmentier (BRGM)
552 calculating the water content in the gas phases with the Simulis© Thermodynamics code.
553 They are grateful to all of the project partners (TOTAL, GDF Suez, Schlumberger, Itasca,
554 CNRS, University de Lorraine, University of Pau) for authorizing the publication of this work.

555

556 **Appendix A : Governing Transport Equations and Resolution**

557 In TOUGH2 Code, the mass conservation equations governing the flow of multiphase,
558 multicomponent fluids in permeable media can be written in the following form:

$$\frac{d}{dt} \int_{V_n} M^\kappa dV_n = \int_{\Gamma_n} F^\kappa \cdot d\Gamma_n + \int_{V_n} q^\kappa dV_n \quad (A1)$$

559 The integration is over an arbitrary subdomain V_n of the flow system under study, which is
560 bounded by the closed surface Γ_n . The quantity M appearing in the accumulation term (left
561 hand side) represents mass per volume, with $k = 1, \dots, NK$ labeling the components (water,
562 NaCl, CO₂). F denotes mass flux (see below), and q denotes sinks and sources. n is a unit
563 normal vector on surface element $d\Gamma_n$, pointing inward into V_n . Eq. (A1) expresses the fact
564 that the rate of change of fluid mass in V_n is equal to the net inflow across the surface of V_n ,
565 plus net gain from fluid sources.

566 The general form of the accumulation term is:

$$M^\kappa = \phi \sum_{\beta} S_{\beta} \rho_{\beta} X_{\beta}^{\kappa} \quad (A2)$$

567 In Eq. (A2), the total mass of component κ is obtained by summing over the fluid (= liquid,
568 gas) and solid phases β . ϕ is porosity, S_{β} is the saturation of phase β (i.e., the fraction of pore
569 volume occupied by phase β), ρ_{β} is the density of phase β , and X_{β}^{κ} is the mass fraction of
570 component κ present in phase β .

571

572 Advective mass flux is a sum over phases,

$$F^\kappa = \sum_{\beta} X_{\beta}^{\kappa} F_{\beta} \quad (A3)$$

573 and individual phase fluxes are given by a multiphase version of Darcy's law:

$$F_{\beta} = \rho_{\beta} \cdot u_{\beta} = -k \cdot \frac{k_{r\beta} \cdot \rho_{\beta}}{\mu_{\beta}} \cdot (\nabla P_{\beta} - \rho_{\beta} \cdot g) \quad (A4)$$

575 Here u_{β} is the Darcy velocity (volume flux) in phase β , k is absolute permeability, $k_{r\beta}$ is
576 relative permeability to phase β , μ_{β} is viscosity, and P_{β} (the fluid pressure in phase β) is the
577 sum of the pressure P of a reference phase (usually taken to be the gas phase), and the
578 capillary pressure $P_{c\beta}$ (≤ 0). g is the vector of gravitational acceleration. TOUGH2 simulator
579 also considers diffusive fluxes in all phases, and includes coupling between diffusion and
580 phase partitioning that can be very important for volatile solutes in multiphase conditions
581 (Pruess, 2002). Diffusive flux of component κ in phase β is given by

$$f_{\beta}^{\kappa} = -\phi \tau_0 \tau_{\beta} \rho_{\beta} d_{\beta}^{\kappa} \nabla X_{\beta}^{\kappa} \quad (A5)$$

582 where $\tau_0 \tau_{\beta}$ is the tortuosity which includes a porous medium dependent factor τ_0 and a
583 coefficient that depends on phase saturation S_{β} , $t_{\beta} = t_{\beta}(S_{\beta})$, and d_{β}^{κ} is the diffusion coefficient

584 of component κ in bulk fluid phase β . Special TOUGH2 versions that include a conventional
585 Fickian model for hydrodynamic dispersion have also been developed, but this option is not
586 activated in the present study (see § 4.2 for more explanations).

587 By applying Gauss' divergence theorem, equation (A1) can be converted into the following
588 Partial Differential Equation (PDE):

$$\frac{dM^\kappa}{dt} = -div F^\kappa + q^\kappa \quad (A6)$$

589 which is the form commonly used as the starting point for deriving finite difference or finite
590 element discretization approaches. However, in TOUGH2 an "integral finite difference"
591 method (Narasimhan and Witherspoon, 1976) is used, in which space discretization is
592 directly applied to the integrals in Eq. (A1).

593 The calculation of thermophysical properties for water/NaCl/CO₂ mixtures appearing in the
594 equations given above is described in the ECO2n user's guide (Pruess, 2005).

595 **Appendix B : Details about precipitation/dissolution of sodium chloride**

596 The TOUGH2 code includes several Equation of State (EOS) modules developed specifically
597 for treating different mixtures in order to solve problems in the fields of hydrogeology,
598 geothermal and petroleum engineering, nuclear waste disposal, and environmental pollution
599 (Pruess, 1999). The ECO2n EOS module (Pruess, 2005) was developed to simulate flow
600 problems in which the transport of a variable salinity brine and a Non Condensable Gas (CO₂)
601 occurs. The multiphase system is assumed to be composed of three mass components:
602 water, sodium chloride, and carbon dioxide. Whereas water and CO₂ components may be
603 present only in the liquid and gas phases, the salt component may be dissolved in the liquid
604 phase or precipitated to form a solid salt phase.

605 The treatment of precipitation/dissolution of sodium chloride has been introduced using the
606 method employed to treat similar phenomena occurring for water-silica mixtures (Verma and
607 Pruess, 1988). Dissolved salt concentration is characterized in ECO2n module by means of
608 a specific primary variable x_{NaCl} (fraction of total H₂O+NaCl mass). This variable is restricted
609 to the range $0 \leq x_{NaCl} \leq x_{eq}$, where x_{eq} is the solubility of salt according to temperature (Potter
610 et al. 1977, Chou 1987):

$$611 \quad x_{eq} = 0.26218 + 7.2 \cdot 10^{-5} \cdot T + 1.06 \cdot 10^{-6} \cdot T^2 \quad (B1)$$

612 with T in °C. When salt concentration (x_{NaCl}) exceeds salt solubility (x_{eq}), this corresponds to
613 conditions in which solid salt will be present in addition to dissolved salt in the aqueous
614 phase. The mass of precipitated salt is then calculated and used to evaluate the reduction of
615 rock porosity, as well as the related formation permeability, according to relationships given
616 in the text (see § 4.1).

617

618 **References**

- 619 Alkan, H., Cinar, Y., Ülker, E. B., 2010. Impact of Capillary Pressure, Salinity and In situ
620 Conditions on CO₂ Injection into Saline Aquifers. *Transport in Porous Media* 84, 799–
621 819.
- 622 André, L., Audigane, P., Azaroual, M., Menjz, A., 2007. Numerical modeling of fluid-rock
623 chemical interactions at the supercritical CO₂-liquid interface during supercritical carbon
624 dioxide injection into a carbonated reservoir, the Dogger aquifer (Paris Basin, France).
625 *Energy Conversion and Management* 48, 1782-1797.
- 626 André, L., Azaroual, M., Menjz, A., 2010. Numerical Simulations of the Thermal Impact of
627 Supercritical CO₂ Injection on Chemical Reactivity in a Carbonate Saline Reservoir.
628 *Transport in Porous Media* 82 (1), 247-274.
- 629 Audigane, P., Gaus, I., Czernichowski-Lauriol, I., Pruess, K., Xu, T., 2007. Two-dimensional
630 reactive transport modeling of CO₂ injection in a saline Aquifer at the Sleipner site,
631 North Sea. *American Journal of Science* 307, 974-1008.
- 632 Bennion, B., Bachu, S., 2005. Relative permeability characteristics for supercritical CO₂
633 displacing water in a variety of potential sequestration zones in the Western Canada
634 sedimentary basin. SPE 95547. SPE Annual Technical Conference and Exhibition,
635 Dallas, USA, 9-12 October 2005.
- 636 Bielinski, A., Kopp, A., Schütt, H., Class, H., 2008. Monitoring of CO₂ plumes during storage
637 in geological formations using temperature signals: numerical investigation.
638 *International Journal of Greenhouse Gas Control* 2, 319-328.
- 639 Chiquet, P., Daridon, J.L., Broseta, D., Thibeau, S., 2007. CO₂/water interfacial tensions
640 under the pressure and conditions of geological storage. *Energy Conversion and*
641 *Management* 48, 736–744.
- 642 Chalbaud, C., Robin, M., Lombard, J.-M., Egermann, P., Bertin, H., 2009. Interfacial tension
643 measurements and wettability evaluation for geological CO₂ storage, *Advances in*
644 *Water Resources* 32, 98–109.

645 Chou, I.-M., 1987. Phase relations in the system NaCl-KCl-H₂O. III: Solubilities of halite in
646 vapor-saturated liquids above 445°C and redetermination of phase equilibrium
647 properties in the system NaCl-H₂O to 1000°C and 1500 bars. *Geochimica*
648 *Cosmochimica Acta* 51, 1965-1975.

649 Corey, A.T., 1954. The interrelation between gas and oil relative permeabilities. *Producers*
650 *Monthly*, 38-41, November 1954.

651 Egermann, P., Chalbaud, C., Duquerroix, J.-P., Le Gallo, Y., 2006. An Integrated Approach
652 to Parameterize Reservoir Models for CO₂ Injection in Aquifers. SPE 102308. SPE
653 Annual Technical Conference and Exhibition, San Antonio, USA, 24-27 September
654 2006.

655 Ennis-King, J., Paterson, L., 2007. Coupling of geochemical reactions and convective mixing
656 in the long-term geological storage of carbon dioxide. *International Journal of*
657 *Greenhouse Gas Control* 1 (1), 86–93.

658 Giorgis, T., Carpita, M., Battistelli, A., 2007. 2D modeling of salt precipitation during the
659 injection of dry CO₂ in a depleted gas reservoir. *Energy Conversion and Management*
660 48, 1816-1826.

661 Huq, F., Blum, P., Marks, M.A.W., Nowak, M., Haderlein, S.B., Grathwohl, P., 2012.
662 Chemical changes in fluid composition due to CO₂ injection in the Altmark gas field:
663 preliminary results from batch experiments. *Environmental Earth Sciences* 67 (2), 385-
664 394.

665 Hurter, S., Labregere, D., Berge, J., 2007. Simulations for CO₂ injection projects with
666 compositional simulator. SPE 108540. Offshore Europe 2007 Conference, Aberdeen,
667 Scotland, 4-7 September 2007.

668 Kim, M., Sell, A., Sinton, D., 2013. Aquifer-on-a-chip: understanding pore-scale salt
669 precipitation dynamics during CO₂ sequestration. *Lab on a chip*,
670 doi:10.1039/c3lc00031a.

671 Kleinitz, W., Tölcke, W., 1982. Bildungsbedingungen von Ablagerungen in Gasbohrungen
672 und deren Beseitigung; *Erdöl-Erdgas-Zeitschr.*, 4.

673 Kleinitz, W., Koehler, M., Dietzsch, G., 2001. The Precipitation of Salt in Gas Producing
674 Wells. SPE 68953. SPE European Formation Damage Conference, The Hague, The
675 Netherlands, 21–22 May 2001.

676 Kleinitz, W., Dietzsch, G., Köhler, M., 2003. Halite scale formation in gas producing wells.
677 Chemical Engineering Research and Design 81 (PartA).

678 Kopp, A., Ebigbo, A., Bielinski, A., Class, H., Helmig, R., 2009. Numerical simulation of
679 temperature changes caused by CO₂ injection in geological reservoirs. in M. Grobe, J.
680 C. Pashin, and R. L. Dodge, eds., Carbon dioxide sequestration in geological media—
681 State of the science: AAPG Studies in Geology 59, 439–456.

682 Leroy, P., Lassin, A., Azaroual, M., André, L., 2010. Predicting the surface tension of
683 aqueous 1:1 electrolyte solutions at high salinity. Geochimica and Cosmochimica Acta
684 74, 5427-5442.

685 Mahadevan, J., 2005. Flow-through drying of porous media. PhD Dissertation. The University
686 of Texas at Austin.

687 Mahadevan, J., Sharma, M.M., Yortsos, Y.C., 2007. Water removal from porous media by
688 gas injection: experiments and simulation. Transport in Porous Media 66, 287-309.

689 Mehnert, E., Okwen, R.T., 2012. Near-well pressure distribution of CO₂ injection in a partially
690 penetrating well. Proceedings of TOUGH Symposium 2012, Lawrence Berkeley
691 National Laboratory, Berkeley, California, 17-19 September 2012.

692 Narasimhan, T.N., Witherspoon P. A., 1976. An integrated finitedifference method for
693 analyzing fluid flow in porous media. Water Resources Research 12(1), 57– 64.

694 Okwen, R.T., Stewart, M.T., Cunningham, J.A., 2011. Temporal variations in near-wellbore
695 pressures during CO₂ injection in saline aquifers. International Journal of Greenhouse
696 Gas Control 5(5), 1140-1148.

697 Oldenburg, C.M., Moridis, G.J., Spycher, N., Pruess, K., 2004. EOS7C Version 1.0:
698 TOUGH2 Module for Carbon Dioxide or Nitrogen in Natural Gas (Methane) Reservoirs.
699 Lawrence Berkeley National Laboratory Report LBNL-56589, Berkeley, CA (USA).

700 Ott, H., de Kloe, K., Marcelis, F., Makurat, A., 2010a. Injection of Supercritical CO₂ in Brine
701 Saturated Sandstone: Pattern Formation during Salt Precipitation. Energy Procedia 4,
702 4425-4432.

703 Ott, H., de Kloe, K., Taberner, C., Marcelis, F., Wang, Y., Makurat A., 2010b. Rock/fluid
704 interaction by injection of Supercritical CO₂/H₂S : Investigation of dry-zone formation
705 near the injection well. International Symposium of the Society of Core Analysts
706 (SCA2010-20), Halifax, Nova Scotia, Canada, 4-7 October 2010.

707 Peter-Borie, M., Blaisonneau, A., Gentier, S., Rachez, X., Shiu, W., Dedecker, F., 2011. A
708 particulate rock model to simulate thermo-mechanical cracks induced in the near-well
709 by supercritical CO₂ injection. Annual Conference of the International Association for
710 Mathematical Geosciences, Salzburg, Austria, 5-9 September 2011.

711 Peysson, Y., Bazin, B., Magnier, C., Kohler, E., Youssef, S., 2010. Permeability alteration
712 due to salt precipitation driven by drying in the context of CO₂ injection. International
713 Conference on Greenhouse Gas Technologies (GHGT-10), Amsterdam, 19-23
714 September 2010.

715 Peysson, Y., 2012. Permeability alteration induced by drying of brines in porous media. The
716 European Physical Journal - Applied Physics 60, 24206p1-p12.

717 Peysson, Y., André, L., Azaroual, M., 2013. Well injectivity during CO₂ injection in deep saline
718 aquifers -Part 1: Experimental investigations of drying effects and salt precipitation.
719 International Journal of Greenhouse Gas Control, same issue.

720 Potter, R.W., Babcock, R.S., Brown, D.L., 1977. A new method for determining the solubility
721 of salts in aqueous solutions at elevated temperatures. Journal of Research of the U. S.
722 Geological Survey 5(3), 389-395.

723 Pruess, K., Oldenburg, C.M., Moridis, G.J., 1999. TOUGH2 User's Guide, Version 2.0.
724 Lawrence Berkeley National Laboratory Report LBNL-43134, Berkeley, CA (USA).

725 Pruess, K., 2002. Numerical simulation of multiphase tracer transport in fractured geothermal
726 reservoirs, Geothermics 31, 475-499.

727 Pruess, K., 2005. ECO2n: a TOUGH2 fluid property module for mixtures of water, NaCl and
728 CO₂. Lawrence Berkeley National Laboratory Report LBNL-57952, Berkeley, CA
729 (USA).

730 Pruess, K., Müller, N., 2009. Formation dry-out from CO₂ injection into saline aquifers: 1.
731 Effects of solids precipitation and their mitigation, Water Resources Research, 45,
732 W03402

733 Soreide, I., Whitson, C.H, 1992. Peng–Robinson predictions for hydrocarbons, CO₂, N₂, and
734 H₂S with pure water and NaCl brine. Fluid Phase Equilibria 77, 217–240.

735 Sterpenich, J., Renard, S., Pironon, J., 2006. Reactivity of French Triassic sandstones
736 submitted to CO₂ under deep geological storage conditions. In Proceeding of 8th
737 International Conference on Greenhouse Gas Control Technologies, 19-22 June 2006,
738 Trondheim, Norway.

739 Van Genuchten, M.T., 1980. A closed-form equation for predicting the hydraulic conductivity
740 of unsaturated soils. Soil Science Society of America Journal 44, 892-898.

741 Vandeweyer, V., Van der Meer, B., Hofstee, C., 2011. Monitoring the CO₂ injection site : K12-
742 B. Energy Procedia 4, 5471-5478.

743 Verma, A., Pruess, K., 1988. Thermohydrologic conditions and silica redistribution near high-
744 level nuclear wastes emplaced in saturated geological formations. Journal of
745 Geophysical Research 93 (B2), 1159– 1173.

746 Vilarrasa, V., 2012. Thermo-Hydro-Mechanical Impacts of Carbon Dioxide(CO₂) Injection in
747 Deep Saline Aquifers. PhD Thesis. Department of Geotechnical Engineering and
748 Geosciences, Civil Engineering School, Technical University of Catalonia, GHS, UPC,
749 Barcelona, Spain.

750 Wagner, W., Pruss, A., 2002. The IAPWS formulation 1995 for the thermodynamic properties
751 of ordinary water substance for general and scientific use. Journal of Physical and
752 Chemical Reference Data 31 (2), 387-535.

753 Xu, T., Ontoy, Y., Molling, P., Spycher, N., Parini, M., Pruess, K., 2004. Reactive transport
754 modeling of injection well scaling and acidizing at Tiwi Field, Philippines. *Geothermics*
755 33(4), 477 – 491.

756 Zeidouni, M., Pooladi-Darvish, M., Keith, D., 2009. Analytical solution to evaluate salt
757 precipitation during CO₂ injection in saline aquifers. *International Journal of*
758 *Greenhouse Gas Control* 3, 600–611.

759

760

List of figures

761

762

763 Figure 1 – Gas (k_{rg}) and water (k_{rl}) relative permeability curves (left) and capillary pressure
764 curve (right) for Vosges Sandstone samples (IFPEN Data)

765 Figure 2 - Experimental procedure to study the drying-out of a sandstone core under a
766 continuous flux of anhydrous gas

767 Figure 3 - Molar fraction of water (y_{H_2O}) in the gas phase at 80°C according to pressure.

768 Figure 4 - Mean water content in the core and outlet gas flux (at 80°C): symbols are
769 measured data and lines are calculated values

770 Figure 5 - Relationship between porosity and permeability reduction, from Verma and
771 Pruess (1988) optimized for Vosges Sandstone ($\Pi = 0.8$ and $\phi_r = 0.91$) where Π is the
772 fractional length of pore bodies and ϕ_r is the fraction of initial porosity for which permeability
773 is reduced to zero. K and ϕ are permeability and porosity at time t , respectively, and subscript
774 0 indicates the initial values of these two rock parameters.

775 Figure 6 - Modelling results for the variations in permeability inside the core during CO_2
776 injection, for gas injection with increasing pressure steps (solid grey line) and for a constant
777 pressure gradient (dotted grey line).

778 Figure 7 – Comparison between measured X-ray adsorption (back line – Peysson et al.,
779 2013) and the calculated amounts of salt deposits for gas injection by increasing
780 pressure steps (solid grey line) and for a constant pressure gradient (dotted grey line).

781 Figure 8 - Permeability variations around the injection well depending on brine salinity, for the
782 same pressure gradient ($\Delta P = 2$ bars). k_{-red} ($= K/K_0$) is the permeability reduction according
783 to time. K_0 is the initial permeability and K is the permeability at time t

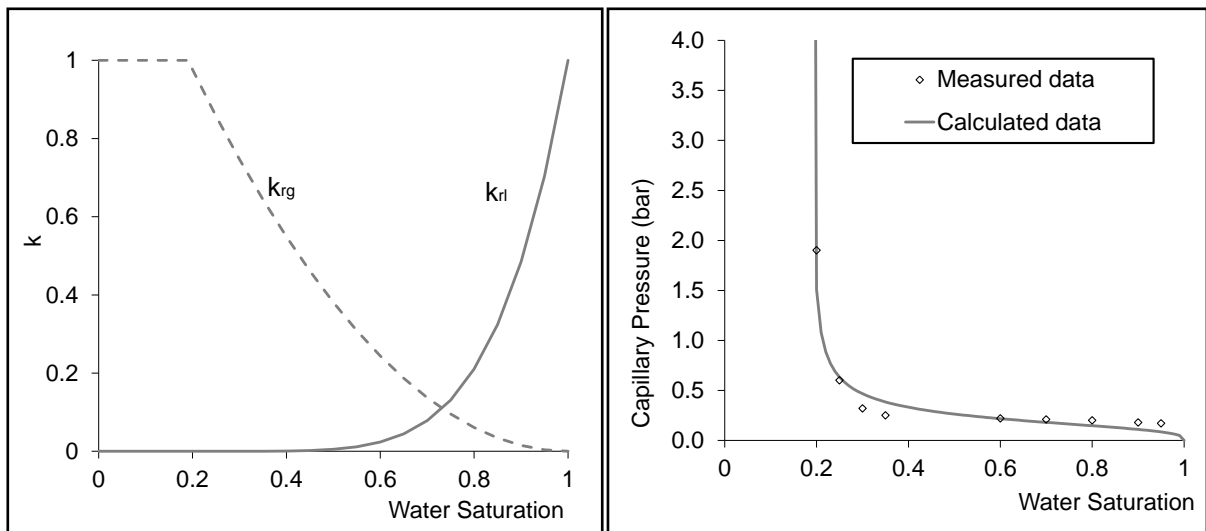
784 Figure 9–(a) Permeability variations close to the injection well as a function of the injection
785 flow rate for three initial brine salinities (between 10 and 160 g/L); (b) Prediction of the risk of
786 clogging close to the injection well depending on the injection flow rate and Peclet number

787 Figure 10 - (a) Gas Saturation (SG), (b) Solid Saturation (SS) (= precipitated salt volume/pore
788 volume), and (c) permeability reduction ($k_{red} = K/K_0$) within a 100 m radius around the
789 injector after ten years of supercritical CO₂ injection, where K_0 is the initial permeability

790 Figure 11 - Gas (a) and brine (b) fluxes within a 100 m radius around the injector after ten
791 years of supercritical CO₂ injection. The lengths of the flow vectors (drawn at the center of
792 each grid cell) are proportional to the intensity of the flow. Arrows indicate flow direction.

793 Figure 12 - Conceptual model of the main fluxes inside a homogeneous reservoir during
794 supercritical CO₂ injection

795

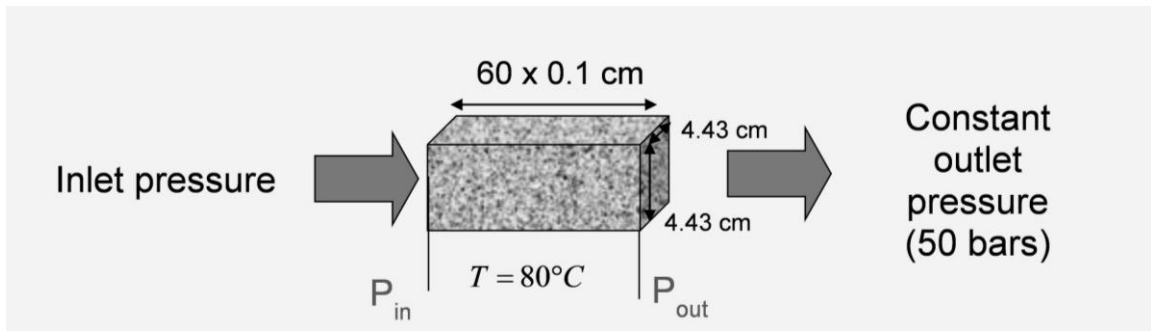


796

797

Figure 1

798

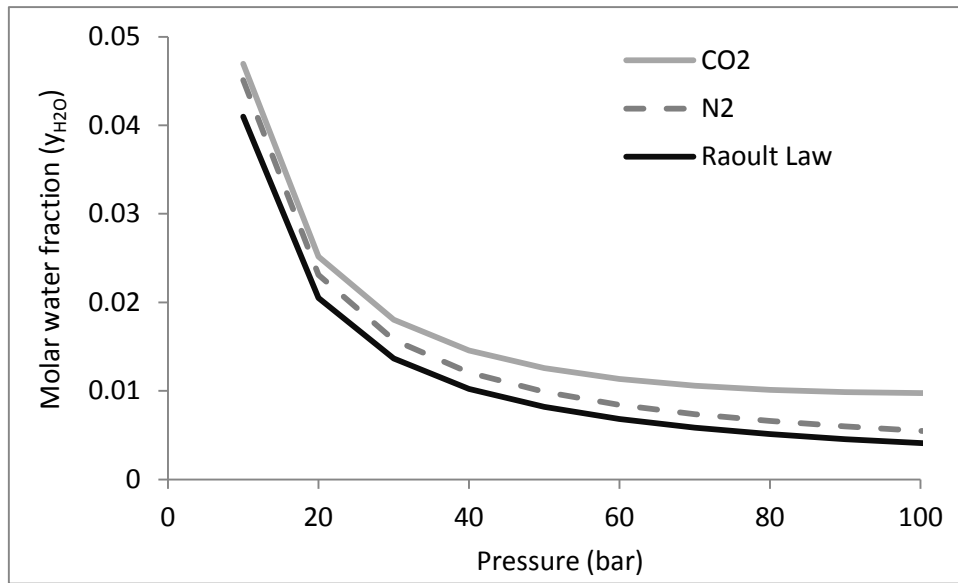


799

800

801

Figure 2



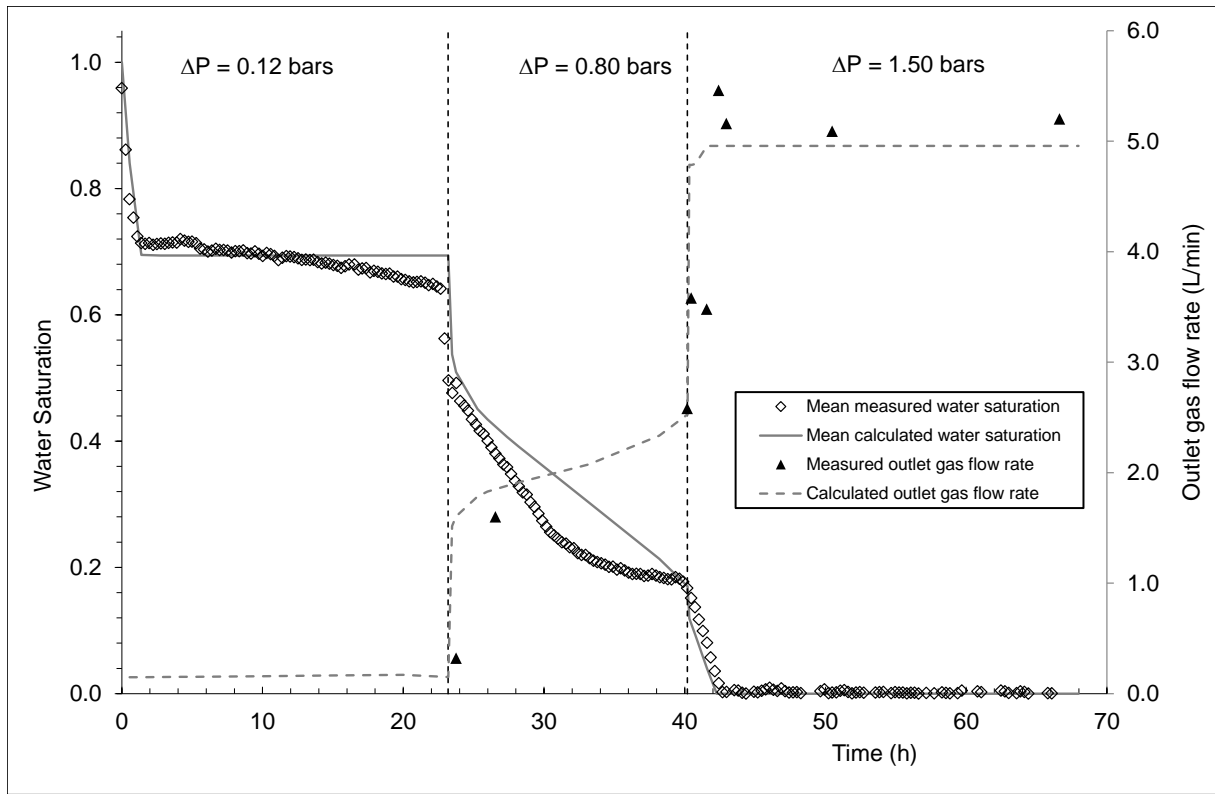
802

803

804

805

Figure 3

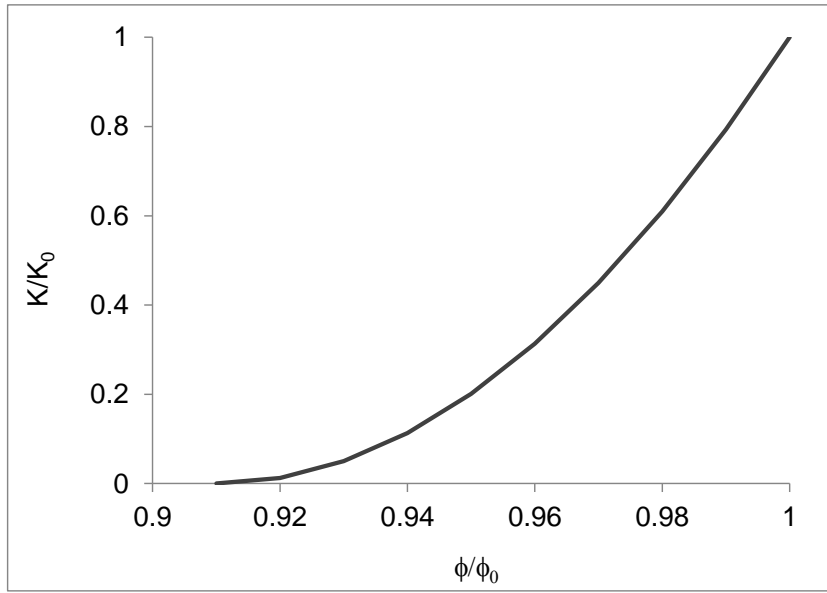


806

807

Figure 4

808

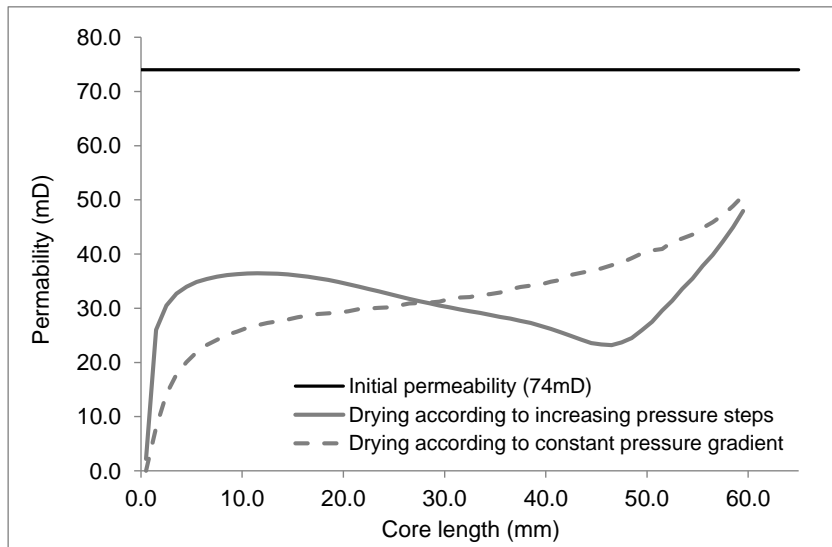


809

810

Figure 5

811

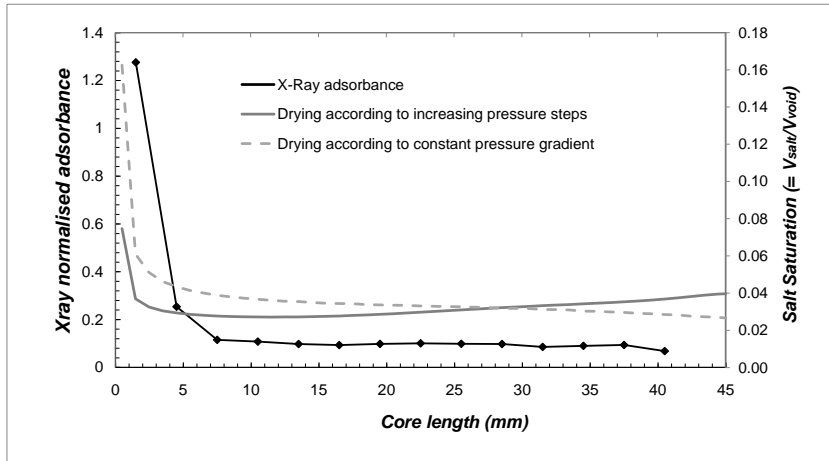


812

813

Figure 6

814



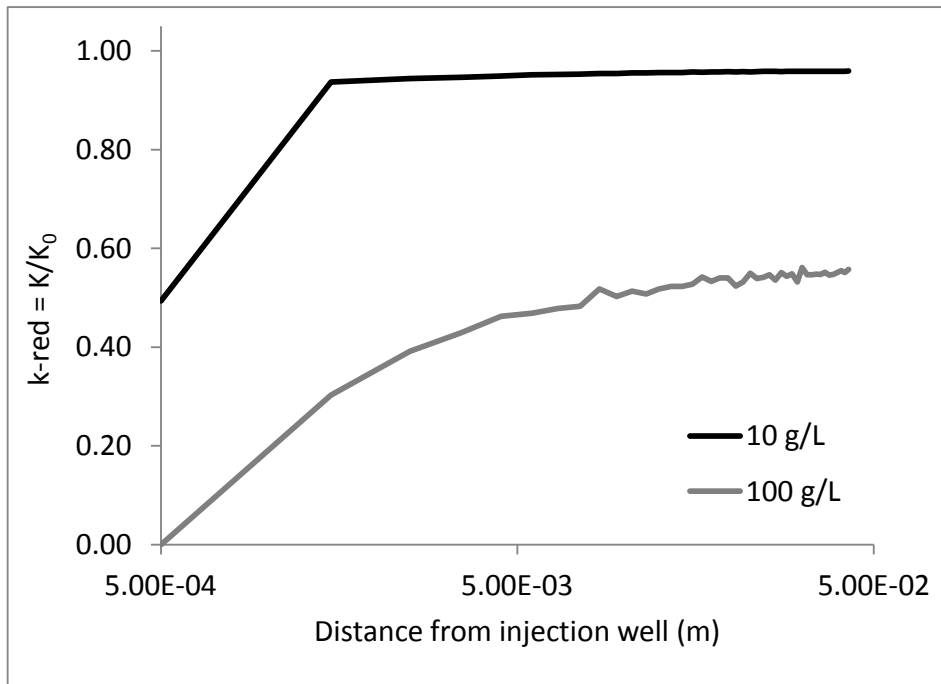
815

816

Figure 7

817

818



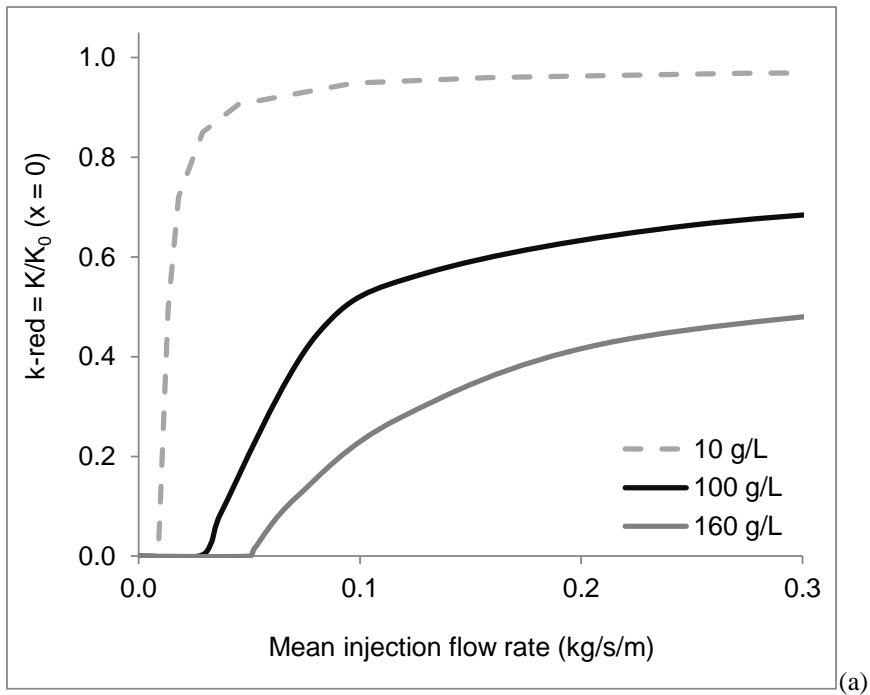
819

820

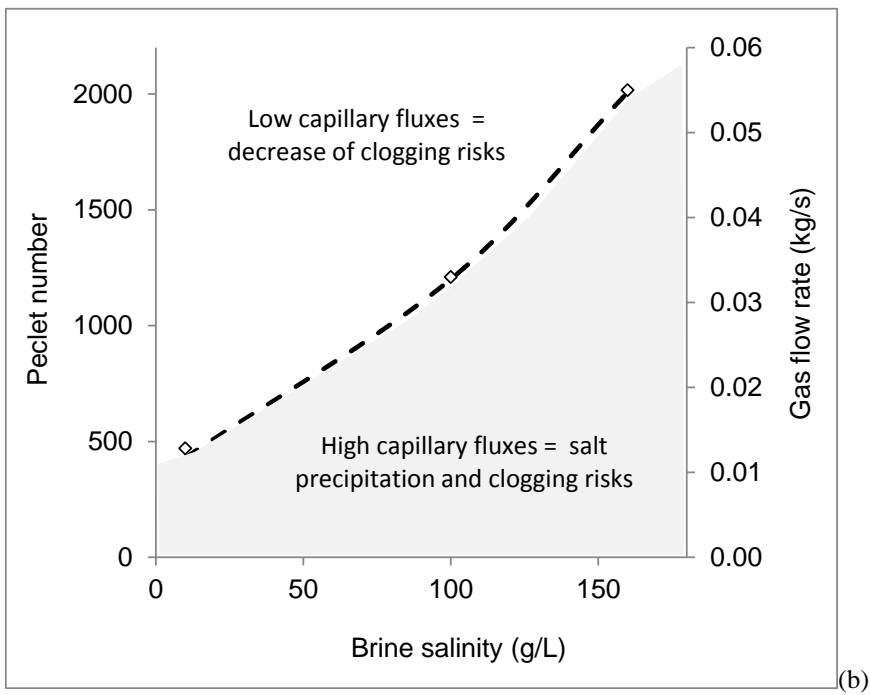
821

822

Figure 8



823

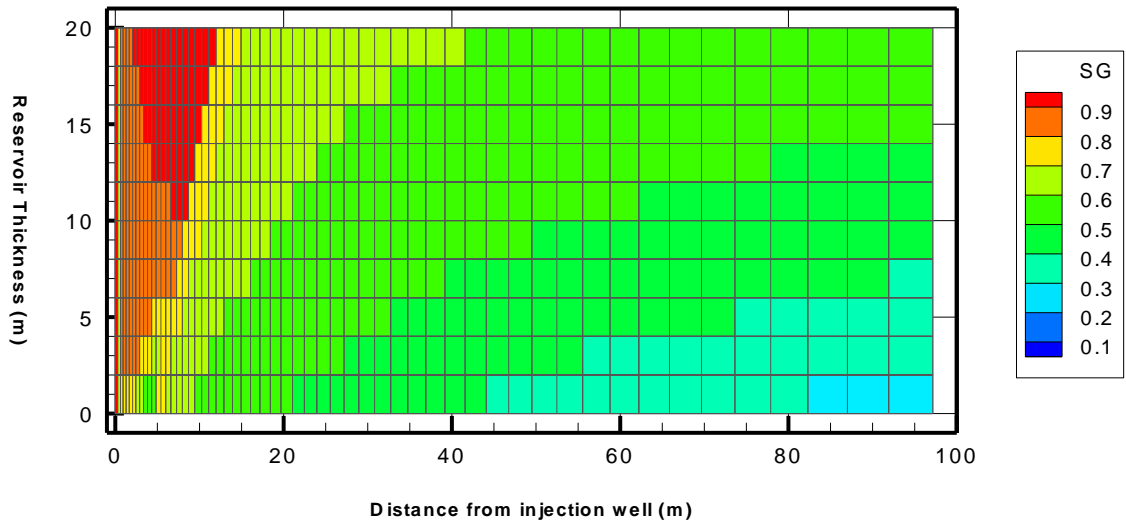


824

825

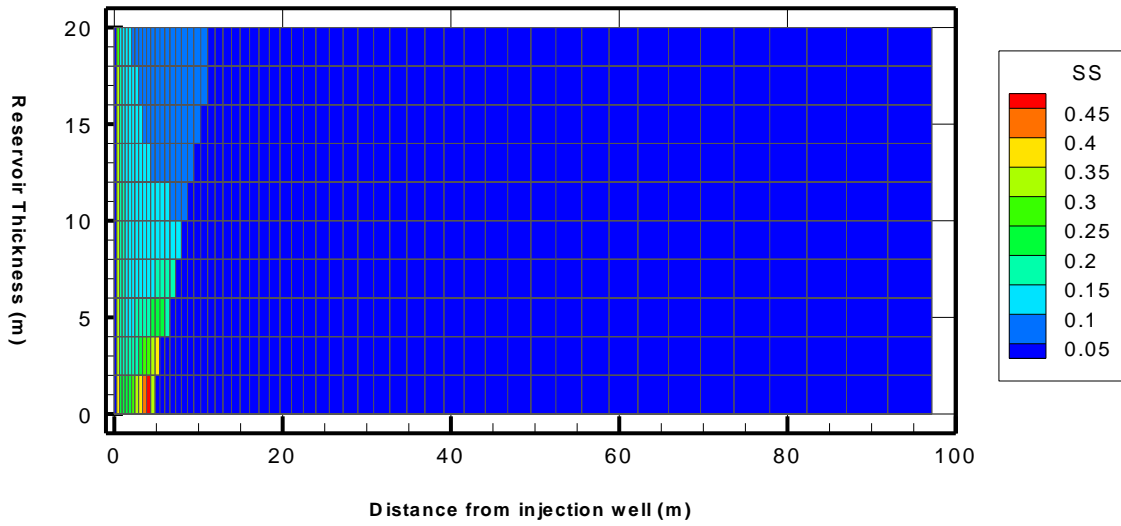
826

Figure 9

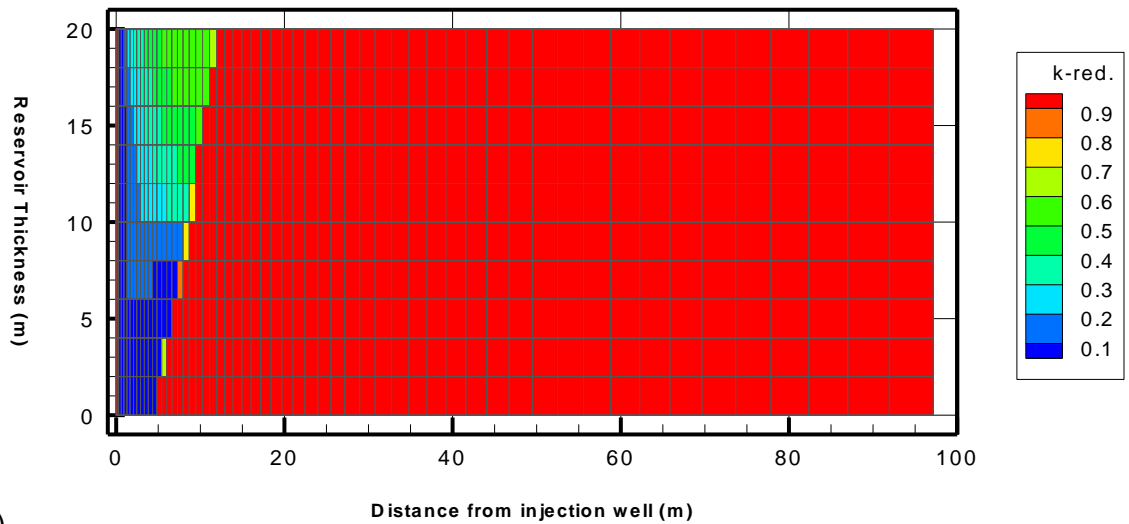


827
828

(a)



829



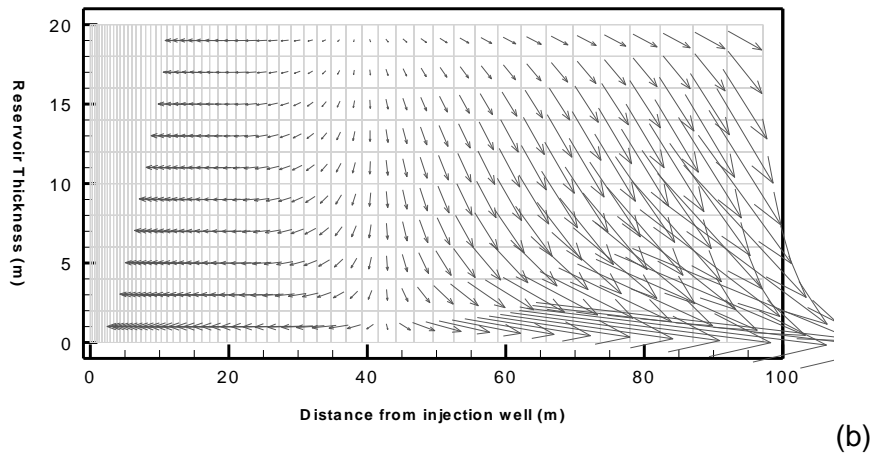
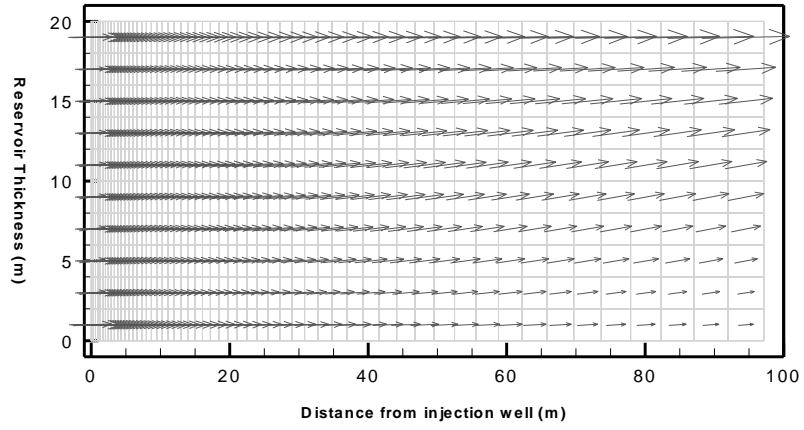
830 (b)

(c)

831

832

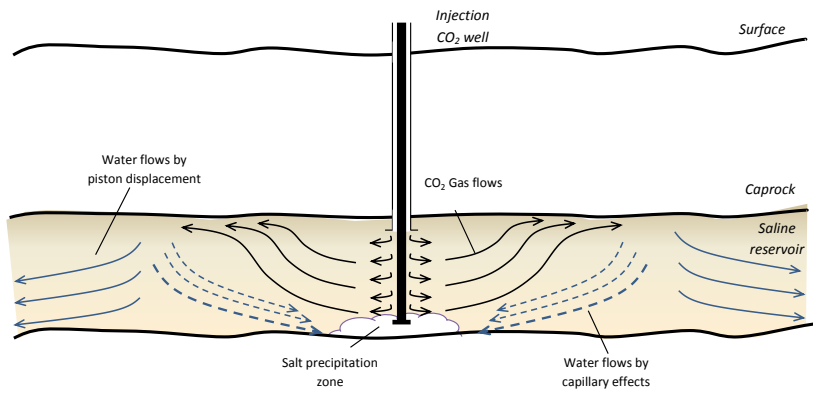
Figure 10



836

Figure 11

837



838

839

Figure 12

840

841